Assessment of Subsampling Schemes for Compressive Nano-FTIR Imaging

Selma Metzner, Bernd Kästner, Manuel Marschall, Gerd Wübbeler, Stefan Wundrack, Andrey Bakin, Arne Hoehl, Eckart Rühl, and Clemens Elster

***Abstract*— Nano-Fourier transform infrared (FTIR) imaging is a powerful scanning-based technique at nanometer spatial resolution that combines FTIR spectroscopy and scattering-type scanning near-field optical microscopy (s-SNOM). Recording large spatial areas using nano-FTIR is, however, limited, because its sequential data acquisition entails long measurement times. Compressed sensing and low-rank matrix reconstruction are mathematical techniques that can reduce the number of these measurements significantly by requiring only a small fraction of randomly chosen measurements. However, choosing this small set of measurements in a random fashion poses practical challenges for scanning procedures and does not save as much time as desired. We, therefore, consider different subsampling schemes of practical relevance that ensure rapid data acquisition, much faster than random subsampling, in combination with a low-rank matrix reconstruction procedure. It is demonstrated that the quality of the results for almost all subsampling schemes considered, namely, original Lissajous, triangle Lissajous, and random reflection subsampling, is similar to that achieved for random subsampling. This implies that nano-FTIR imaging can be significantly extended to also cover samples extended over large areas while maintaining its high spatial resolution.**

***Index Terms*— Lissajous, low-rank matrix reconstruction, nano-Fourier transform infrared (FTIR), subsampling.**

I. Introduction

INFRARED (IR) spectroscopy is a nondestructive technique for material characterization used in fields ranging from analytical chemistry [1], [2], materials sciences [3], [4], and life sciences [5], [6], [7] to microelectronics [8]. While the spatial resolution of conventional IR microscopy is limited to several micrometers due to the diffraction limit [9], this limitation can be overcome by modern scanning probe microscopy-based methods that apply, for instance, near-field-based techniques. Examples include scattering-type scanning near-field optical microscopy (s-SNOM) [10], [11], atomic force microscopy-based IR spectroscopy (AFM-IR) [12], [13], photoinduced force microscopy (PiFM) [14], tip-enhanced photoluminescence (TEPL) spectroscopy [15], and tip-enhanced Raman spectroscopy (TERS) [16].

Nano-Fourier transform IR (FTIR) [17], [18] is another scanning-based technique that combines FTIR spectroscopy and s-SNOM. Here, FTIR spectroscopy uses a broadband IR source, such as tunable lasers, thermal, or synchrotron radiation. Spatial resolution is enhanced in s-SNOM by incorporating the principle of atomic force microscopy. Nano-FTIR allows the complete spectrum at each pixel of the scanned area to be acquired with nanoscale spatial resolution. Typical applications of nano-FTIR range from the mapping of semiconductors [19] to molecular fingerprinting [20].

Usually, such scanning-based approaches take the spectra in a sequential process, resulting in long acquisition times for extended 2-D arrays. These scans may take several hours to achieve nanometer spatial resolution over a substantial field of view in the micrometer size regime. Such long acquisition times may also lead to sample and tip damage as well as drift artifacts.

Several methods have been presented to overcome long acquisition times, e.g., in the fields of magnetic resonance imaging (see, for example, [21]) and scanning probe microscopy [22]. For nano-FTIR, a compressed sensing approach was introduced in [23]. Its potential benefit was demonstrated by reconstruction results achieved for nano-FTIR measurements when using only 11% of the original data. Alternatively, a number of low-rank matrix reconstruction algorithms were developed by [24], [25], [26], and [27], in which they show that their methods require only a small fraction of less than 10% of all measurements, which could, in principle, reduce the experimental effort significantly. However, the reduced set of measurements was chosen randomly. In practical terms, this implies that each single measurement position needs to be accessed individually, thereby also passing along idle routes and positioning times during which no measurement is carried out. Consequently, the time saved is less than that desired.

In this work, we introduce several subsampling schemes of practical relevance that subsample experimental data according to specific routes. The acquisition of these data avoids idle routes and is feasible in practical use and much faster than taking the same number of measurements at randomly chosen positions. Motivated by Lissajous curves [28], we develop routes based on 3-D boundary reflection and explore their

Manuscript received 25 April 2022; revised 25 July 2022; accepted 1 August 2022. Date of publication 12 September 2022; date of current version 23 September 2022. This work was supported by the Deutsche Forschungsgemeinschaft under Grant EL 492/1-1 and Grant RU 420/13-1. The work of Bernd Kästner was supported in part by the EMPIR Program through the Participating States and in part by the European Union's Horizon 2020 Research and Innovation Program within the Project 20IND09 PowerElec and 20IND08 MetExSPM. The Associate Editor coordinating the review process was Dr. Xiangchen Qian. *(Corresponding author: Manuel Marschall.)*

Selma Metzner, Bernd Kästner, Manuel Marschall, Gerd Wübbeler, Stefan Wundrack, Arne Hoehl, and Clemens Elster are with the Physikalisch-Technische Bundesanstalt (PTB), Braunschweig and Berlin, 10587 Berlin, Germany (e-mail: manuel.marschall@ptb.de).

Andrey Bakin is with the Institut für Halbleitertechnik, Technische Universität Braunschweig, 38106 Braunschweig, Germany.

Eckart Rühl is with the Physikalische Chemie, Freie Universität Berlin, 14195 Berlin, Germany.

Digital Object Identifier 10.1109/TIM.2022.3204072

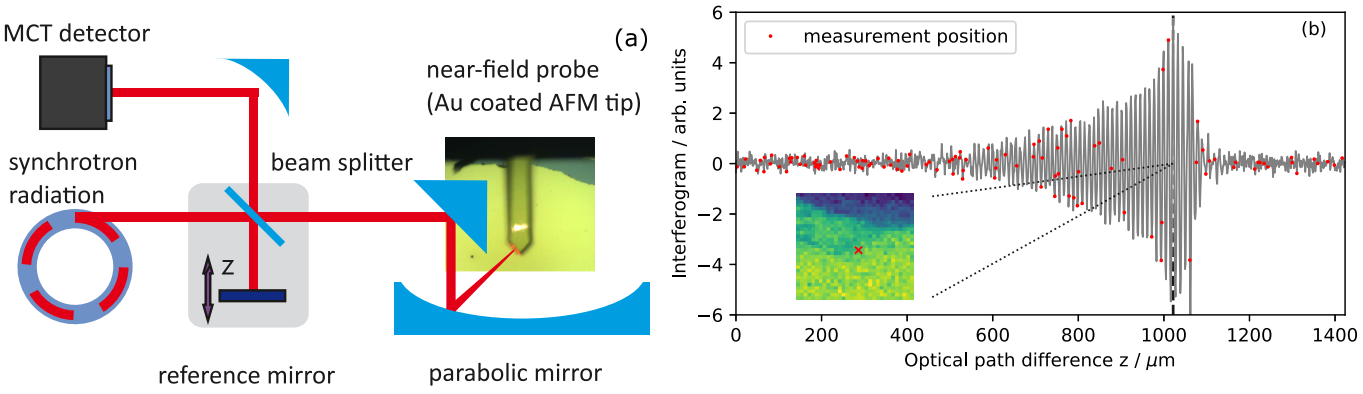

Fig. 1. (a) Nano-FTIR principle. (b) Completely measured interferogram together with randomly chosen measurement positions. The interferogram is obtained at the spatial position indicated by the red cross in the inset domain. The inset itself corresponds to the spatially resolved observation at the interferometer position indicated by the black dashed line at 1021.6 μm.

applicability in nano-FTIR instruments pathing. Using the same low-rank matrix recovery method as in [25], we compare the low-rank reconstructions of the fully sampled dataset for different subsampling schemes with results obtained from random subsampling. The comparison is based on a dataset of a sample corresponding to the edge of an ultrathin gallium film beneath epitaxial graphene grown on 6H-SiC.

This article is organized as follows. In Section II, the measurement process, data preparation, and acquisition are discussed. The numerical low-rank approximation method is presented together with the four subsampling schemes in Section III. Section IV demonstrates the results of different subsampling schemes. Finally, Section V gives some conclusions and an outlook on promising future research topics.

II. Nano-FTIR and Data Acquisition

A. Nano-FTIR

Nano-FTIR is a scanning probe technique based, on the one hand, on FTIR spectroscopy and, on the other hand, on atomic force microscopy. A sharp metallic tip brought close to the sample scans the sample surface and backscatters the incident IR radiation. The metallic tip serves as an optical antenna and strongly restricts the incident optical field to the tip. The near field of the resulting nanoscale light source is then suitable for high-resolution imaging and spectroscopy. To separate the near-field contribution from the far-field background, the backscattered signal is demodulated at the second harmonic of the tip-modulation frequency. The interferogram is recorded by a Michelson interferometer [18], [29] as a function of the optical path difference, and the corresponding spectrum can be obtained from a Fourier transform of the interferogram. A schematic illustration of the experimental approach can be found in Fig. 1(a).

B. Sample and Data Acquisition

As a sample, we chose the edge of an ultrathin gallium film beneath epitaxial graphene on 6H-SiC [30]. The epitaxial graphene was grown on the Si-face of SiC samples (5×10) mm^2 cut from a semi-insulating 6H-SiC wafer with a nominal miscut angle of about 0.06° toward the (1100) plane. The graphene samples were prepared using the polymer-assisted sublimation growth (PASG) technique, which involves polymer adsorbates formed on the SiC surface by liquid-phase deposition from a solution of a photoresist (AZ5214E) in isopropanol followed by sonication and short rinsing with isopropanol. The graphene layer growth was processed at 1750 °C (argon atmosphere ≈1 bar, 6 min, zero argon flow) with pre-vacuum annealing at 900 °C [31], [32]. The PASG method applied allows for the growth of large-area homogeneous monolayer graphene, with almost isotropic resistance characteristics [33]. The fabrication of a large-area 2-D gallium layer at the interface of SiC and graphene has been realized using the liquid metal intercalation technique (LiMIT) [30]. This method achieves the lateral intercalation and diffusion of Ga atoms at room temperature, resulting in the conversion of epitaxial graphene to quasi-freestanding bilayer graphene (QFBLG). The average thickness of the confined gallium layer after the intercalation process is ≈1 nm at the interface between SiC and graphene. In addition, van der Pauw measurements revealed low carrier mobility as well as strong electron doping of $n \approx 4.5 \times 10^{12}$ cm^{-2} in the SiC-confined Ga–QFBLG sample (SiC/2DGa/QFBLG) at room temperature [30].

The structure of the sample results in a strongly resonant phononic spectrum around 920 cm^{-1} as well as a broad metallic spectrum and also exhibits a transition region. Thus, we have a large spectral variation for benchmarking the proposed reconstruction algorithm. A visual representation of the sample is given in Fig. 1(b). We like to point out that the choice of the specimen is not made particularly to favor any subsampling scheme or reconstruction method. However, it serves as a prototype for the general applicability of the methods introduced in the following.

Data acquisition via the Michelson interferometer results in an interferogram $I(z)$ with $N_z = 1024$ equidistant points ($\Delta z \approx 1.39$ μm). The interferogram is converted to a spectrum by Fourier transformation with a spectral resolution of $\Delta\tilde{\nu} = 1/N_z\Delta z \approx 7.03$ cm^{-1}. Altogether, 961 interferograms were recorded on a rectangular area of 2 μm $\times$ 2 μm using a Cartesian grid with 31 $\times$ 31 spatial locations. The fully sam-

pled nano-FTIR dataset can, thus, be represented by a 3-D data cube with the dimensions of $31 \times 31 \times 1024$ recorded within a total measurement time of 170 min. The fully acquired data cube serves as a ground truth to evaluate the reconstruction quality of different subsampling schemes. For the technical demonstration of our approach, the subsampling routes are synthetically applied to this original data cube.

III. Methods

A. Low-Rank Matrix Reconstruction

The concept of low-rank matrices arises in many mathematical settings related to, e.g., modeling and data compression. Applications range from signal processing [34] and image restoration [35] to machine learning [36]. The recovery of a data matrix derived from incomplete observations is a relevant example of a task to which low-rank techniques can be applied. In the case presented here, the data matrix is approximated by a matrix product with each factor having lower dimensionality, resulting in a recovery result of lower rank. The main idea of low-rank matrix reconstruction is that a low-rank approximation already captures the main characteristics of the data, and less informative dimensions are removed. In [25], a low-rank matrix reconstruction was presented and successfully applied to subsampled FTIR data. Specifically, for observations X, the task is to find matrices U and V whose matrix product $\hat{X} = UV^T = \sum_{k=1}^{r} U_{\cdot,k} V_{\cdot,k}$ approximates X. If $r > 0$ is sufficiently small, $\hat{X}$ is called the *low-rank* approximation of X. However, the solution to this decomposition is nonunique. For this reason, and to stabilize the numerical reconstruction, a Tikhonov regularization [37] also accounts for the spatial smoothness of the focal images. The low-rank factors U and V are obtained by minimizing the multilinear objective

$$\left\| X - UV^T \right\|_{\Omega}^2 + \lambda \left(\|\mathrm{KU}\|_2^2 + \|V\|_2^2 \right) \longrightarrow \min$$

where λ is chosen via an L-curve criterion [38], K represents a neighboring matrix, and $\|\cdot\|_{\Omega}$ denotes the Euclidean norm over the index set Ω, which comprises the set of measured points and is subject to the following subsampling schemes. For more details and an in-depth description of the involved variables, we refer to [25], which also includes a step-by-step algorithm description. For comparison reasons, we fix $r = 20$ for which the reconstruction algorithm also terminated with reasonable tolerances.

The resulting minimization problem is solved using an alternating algorithm that generates linear problems in each iteration. An implementation of the Python code employed in this work has been made publicly available [39].

As described earlier, the nano-FTIR data can be represented by a 3-D data cube. The low-rank matrix reconstruction applies to a 2-D object handled in the following way: if X denotes the matrix of measurements for the low-rank matrix reconstruction, then the rows of X indicate the spatial position of the measurements, and the columns of X indicate the interferometer position. Note that, via a one-to-one mapping from 3-D to 2-D, randomly chosen elements of the 3-D data cube correspond to a specified selection of elements of the 2-D matrix.

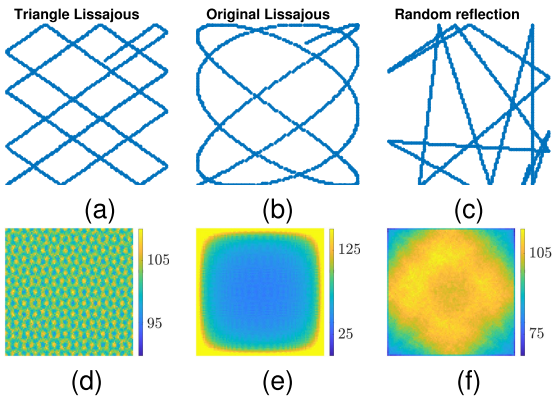

Fig. 2. Visualization of different subsampling schemes. An xy view of the first 1000 sampling points (top row) and the sum of the sampled points along the z-axis (bottom row) for (a) and (d) triangle Lissajous, (b) and (e) original Lissajous, and (c) and (f) random reflection. The colors in (d)–(f) indicate the number of samples in the interferometer direction for each pixel in the xy plane. Note that (e) has a different color scale than (d) and (f).

B. Subsampling Schemes

According to [40], the samples in a data matrix are chosen randomly to avoid information loss when recovering a low-rank matrix. However, the usage of random subsampling does not necessarily lead to significant savings in data acquisition time. For randomly selected nano-FTIR measurements, each sample would need to be approached by nanopositioning systems separately, which is a time-consuming process. In addition, transit times between the samples are not used for measurement. We, therefore, consider routes along which the stages move, which usually occurs in a continuous manner.

In the following, the subsampling schemes considered are listed.

1) Random: A common approach to subsampling is to take a subset randomly selected from the full dataset. We use the term *random* if the samples were selected uniformly along the interferometer axis and within the image plane.

2) Original Lissajous: A 2-D Lissajous curve [41] is the trajectory of a moving point whose coordinates are simple harmonic motions. The parametric equation is given by

$$t \mapsto \begin{pmatrix} A_0 + A\sin(\omega_1 t + \varphi_1) \\ B_0 + B\sin(\omega_2 t + \varphi_2) \end{pmatrix}$$

for $t \in [0, \infty)$. The 2-D Lissajous curves have been applied to scanning techniques, including those in the fields of medical imaging [42], atomic force microscopy [43], [44], and magnetic particle imaging [45]. We will extend the 2-D Lissajous curves to create a 3-D Lissajous path by simply expanding the parametric equation as follows:

$$t \mapsto \begin{pmatrix} A_0 + A\sin(\omega_1 t + \varphi_1) \\ B_0 + B\sin(\omega_2 t + \varphi_2) \\ C_0 + C\sin(\omega_3 t + \varphi_3) \end{pmatrix}.$$

Fig. 2(b) shows an xy view of the first 1000 sampling points along the 3-D Lissajous curve. More details of the employed scheme can be found in the Appendix.

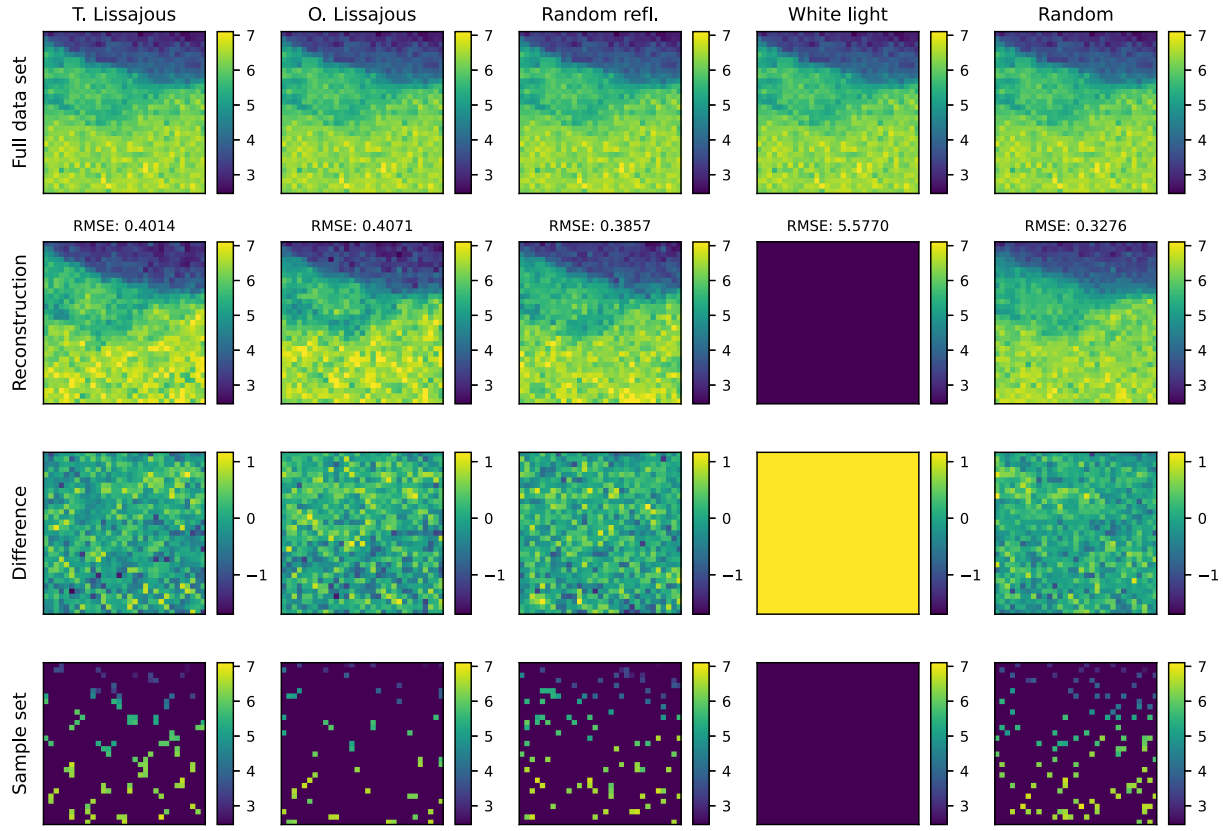

Fig. 3. Reconstruction results for the different subsampling schemes at an interferogram value of 1021.6 μm using 10% of the full data. First column: triangle Lissajous. Second column: original Lissajous. Third column: random reflection. Fourth column: white light. Fifth column: random subsampling. The number above the reconstructed data indicates the root-mean-square error at the interferogram value of 1021.6 μm.

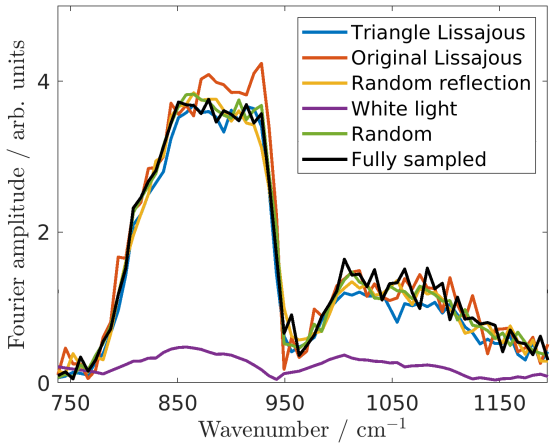

Fig. 4. Reconstructed spectra from 731.1 to 1188.1 cm^{-1} at pixel (4, 25) for the different subsampling schemes. Note that pixel (4, 25) corresponds to point (a) in Fig. 5.

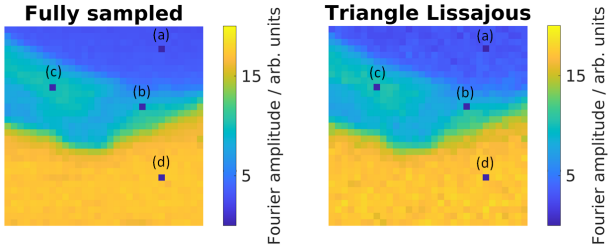

Fig. 5. Amplitude of the spectra at peak position 920.9 cm^{-1} for fully sampled data and subsampled data using a triangle Lissajous scheme. Four different pixel locations (a)–(d) are marked and evaluated in Fig. 6.

3) Triangle Lissajous: Although the samples of original Lissajous are scattered across the entire image stack, sinusoidal waves fail to create a uniform sampling pattern. In Fig. 2(e), the sum along the z-axis of all sample points is shown. Clearly, more samples are located at the border of the image, which could potentially lead to an undesirable biased image reconstruction. In [46], a 3-D *triangle Lissajous* subsampling scheme was introduced for spectroscopic laser-scanning imaging. In Fig. 2(a), an xy view of the first 1000 sampling points along the triangular Lissajous curve is shown. It can be seen [see Fig. 2(d)] that the triangular wave design yields a much more uniform sampling density than the original Lissajous subsampling scheme.

Both the original Lissajous and triangle Lissajous trajectories are sampled in equidistant time steps. For each time step, the interferogram value of the nearest point on the xyz grid is recorded.

4) Random Reflection: Similar to the triangle Lissajous scheme, we consider a so-called *random reflection* subsampling scheme. From a given starting point, the samples are

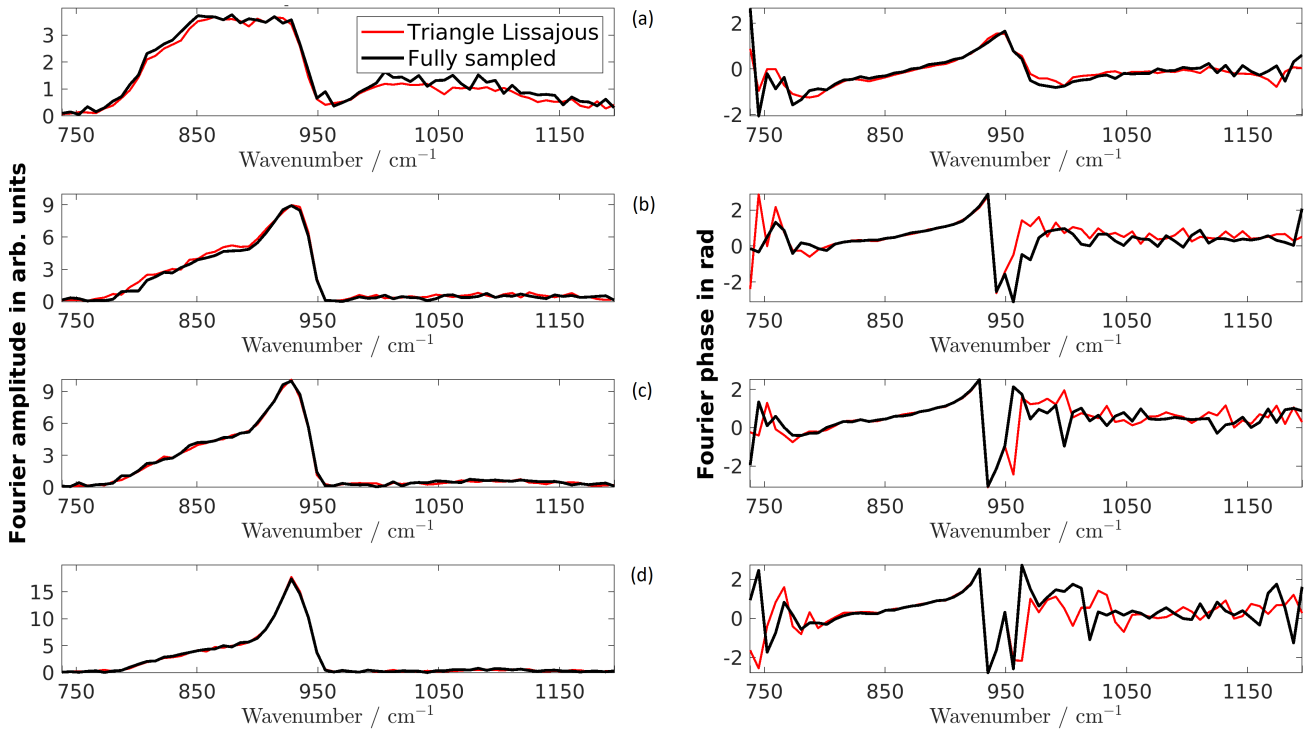

Fig. 6. Amplitude and phase of the reconstructed spectra at different pixel locations for triangle Lissajous subsampling and fully sampled data. The pixel locations in the xy plane are (a) (4, 25), (b) (13, 22), (c) (10, 8), and (d) (24, 25).

acquired along a 3-D line until one of the borders is reached. Then, specified by a random angle, the line is reflected, and new samples can be measured until the next border is reached. This is repeated until the total number of samples is reached. In Fig. 2(c), an example of the xy view of the first 1000 sampling points is shown, while in Fig. 2(f), one can see the sum along the z-axis of all sample points. Compared with the original Lissajous scheme, more samples are now in the center area.

5) White Light: Finally, we introduce the so-called *white light* subsampling scheme. Here, full xy planes are measured, but only for some randomly chosen points along the interferometer axis. This means that, for some points along the z-axis, no points are measured in the image plane, while for others, the entire xy plane is recorded.

IV. Results and Discussion

To test the influence of the different subsampling schemes, five subsets of the full dataset from Section II were created. The points belonging to each subset are chosen according to one of the five subsampling schemes presented earlier using a subsampling rate of 10%.

In the following, we will assess the quality of the low-rank matrix reconstructions in terms of the available full dataset. Here, we specifically want to compare the results when using a random subsampling scheme to the results for the other schemes.

In Fig. 3, the xy planes at the interferogram value of 1021.6 μm are shown for the full dataset, the low-rank reconstructions, the differences between them, and the (subsampled) dataset for each subsampling scheme.

TABLE I

Similarity Measures for the Five Different Low-Rank Reconstructions. Each Value Represents the Average Over the Respective Measure for the Reconstructed Planes From 415.6 to 1166.2 μm

Sub-sampling scheme	Root-mean-square error	Relative error	Correlation coefficient
Triangle Lissajous	0.30	0.48	0.68
Original Lissajous	0.32	0.50	0.66
Random reflection	0.30	0.47	0.68
White light	1.18	0.93	-
Random	0.29	0.46	0.69

A summary of the different similarity measures between the full dataset and low-rank reconstructions can be found in Table I. The relative errors are calculated as $||\hat{X}-X||_F/||X||_F$, where $||\cdot||_F$ denotes the Frobenius norm, and where $\hat{X}$ and X denote the reconstructed and the full dataset, respectively. Note that the correlation coefficient cannot be calculated for white light subsampling, since the reconstruction is 0 everywhere for any z plane where no sample was measured.

While the results of the triangle Lissajous, original Lissajous, and random reflection scheme deliver results similar to a random subsampling scheme, the results from the white light reconstruction are extremely poor.

Note that Fig. 3 refers to an xy plane without samples for the white light subsampling scheme. When looking at the results of the white light subsampling scheme for xy planes that were fully measured, the reconstruction is almost perfect.

In Fig. 4, the resulting spectra from the five reconstructions are shown for pixel (4, 25) and from 731.1 to 1188.1 cm^{-1}

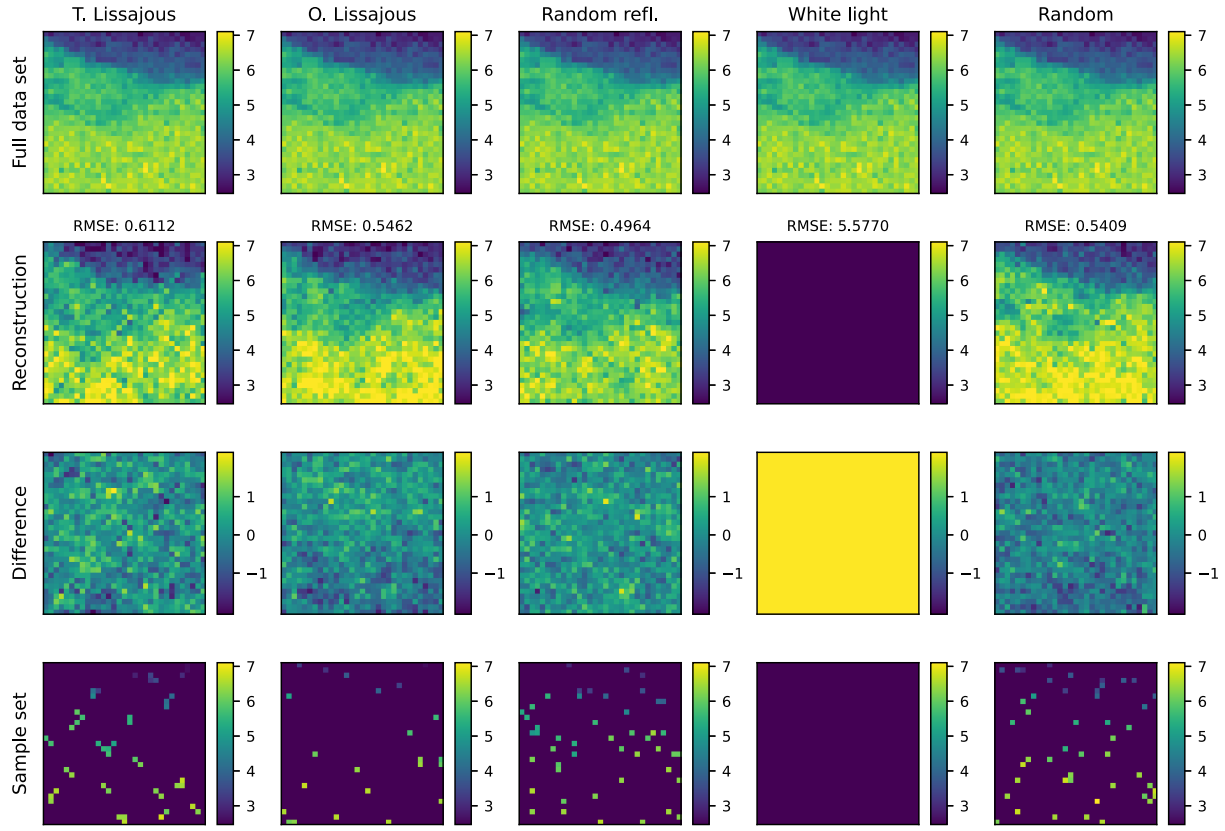

Fig. 7. Reconstruction results for the different subsampling schemes at the interferogram value of 1021.6 μm using 5% of the full data. First column: triangle Lissajous. Second column: original Lissajous. Third column: random reflection. Fourth column: white light. Fifth column: random subsampling.

together with the spectrum of the full dataset. Similar to the abovementioned results, the white light reconstruction is extremely poor, whereas the other subsampling methods yield comparable results. When comparing the random subsampling scheme to the triangle Lissajous and original Lissajous schemes, the spectra are similar to each other.

In Fig. 5, the amplitudes of the spectra at 920.9 cm^{-1} for the fully sampled data and the triangle Lissajous subsampling scheme are shown and appear to be in agreement.

We choose four different points, each characterizing a special part of the spectrum and compare the Fourier amplitude and the Fourier phase of the spectra from 731.1 to 1188.1 cm^{-1} (see Fig. 6). The quality of the low-rank reconstruction for the triangle Lissajous subsampling leads to an agreement to the fully sampled dataset.

To verify that the results for sampling schemes with random elements (i.e., random and random reflection subsampling) are representative, two further, randomly drawn subsets were created for each scheme and used for the reconstruction of the full dataset. Ultimately, the abovementioned results did not change significantly; in particular, we obtained the same numbers as in Table I.

We also created five datasets with a subsampling rate of 5%. Results of the low-rank reconstructions can be seen in Fig. 7. As expected, reducing the amount of data leads to a deterioration in the reconstruction quality. This is also indicated by the increased root-mean-square errors of the reconstructions. Nevertheless, for the triangle Lissajous, original Lissajous, and random reflection schemes, the main features are still clearly visible and comparable to a random subsampling. The white light subsampling still delivers poor results.

Comparing the different subsampling schemes, the random reflection approach yields the smallest overall root-mean-square error of the employed practically relevant sampling schemes. This might be a result of the characteristics of the dataset. Comparing the routes from Fig. 2 with the structure of the sample from Fig. 1(b) indicates that data acquired in the center area sustain more information compared with the boundary area and might even be more important than having a uniform coverage of the sampling domain. Nevertheless, as pointed out in Section II-B, the specimen and application are chosen as a relevant prototype for scanning-based instruments to reflect the general nature of the presented approaches.

V. Conclusion and Outlook

Different subsampling schemes have been compared for compressive nano-FTIR measurement. The triangle Lissajous, original Lissajous, and random reflection schemes have been shown to lead to a suitable data reconstruction for a subsampling rate of 10%. Even with a subsampling rate of 5%, reasonable results were achieved. All three subsampling schemes yielded similar results. Furthermore, these results are in agreement with the results of random subsampling. We have, therefore, presented three subsampling schemes with practical

relevance, which significantly reduced the time required for nano-FTIR measurements.

Future work could apply the subsampling schemes to other nano-FTIR measurements and, due to the general nature of the presented approach, also other scanning probe techniques, which renders our findings relevant for a wider community. Additionally, a hardware implementation of these schemes is necessary to compare the results regarding their acquisition times. We expect that, due to the absence of idle times and the possibility of continuous stage movement, the reduction in acquisition times approaches the subsampling rate.

APPENDIX

A. Details About the Original Lissajous Subsampling Scheme

In Section III-B, a general description of the original Lissajous subsampling scheme is given. In the case presented here for a data cube of dimension $31 \times 31 \times 1024$, the following parameters have been used for the original Lissajous scheme: $A_0 = 15.5$, $B_0 = 15.5$, $C_0 = 512$, $A = 97.3894$, $B = 97.3894$, $C = 3216.9908$, $\omega_1 = 0.0119$, $\omega_2 = 0.0084$, $\omega_3 = 0.0002$, $\varphi_1 = 0.75$, $\varphi_2 = 0.75$, and $\varphi_3 = 0.75$.

ACKNOWLEDGMENT

The authors would like to thank Alexander Govyadinov and Markus Raschke for fruitful discussions.

REFERENCES

[1] R. Salzer and H. W. Siesler, *Infrared and Raman Spectroscopic Imaging*. Hoboken, NJ, USA: Wiley, 2014.

[2] S. Morsch, S. Lyon, S. Edmondson, and S. Gibbon, "Reflectance in AFM-IR: Implications for interpretation and remote analysis of the buried interface," *Anal. Chem.*, vol. 92, no. 12, pp. 8117–8124, Jun. 2020.

[3] F. S. Ruggeri, G. Longo, S. Faggiano, E. Lipiec, A. Pastore, and G. Dietler, "Infrared nanospectroscopy characterization of oligomeric and fibrillar aggregates during amyloid formation," *Nature Commun.*, vol. 6, no. 1, pp. 1–9, Nov. 2015.

[4] J. Chae, Q. Dong, J. Huang, and A. Centrone, "Chloride incorporation process in $CH_3NH_3PbI_{3-x}Cl_x$ perovskites via nanoscale bandgap maps," *Nano Lett.*, vol. 15, no. 12, pp. 8114–8121, 2015.

[5] M. Pilling and P. Gardner, "Fundamental developments in infrared spectroscopic imaging for biomedical applications," *Chem. Soc. Rev.*, vol. 45, no. 7, pp. 1935–1957, Apr. 2016.

[6] I. Hiroaki, N. Toyonori, and T. Eiji, "Measurement of pesticide residues in food based on diffuse reflectance IR spectroscopy," *IEEE Trans. Instrum. Meas.*, vol. 51, no. 5, pp. 886–890, Oct. 2002.

[7] M. A. Pleitez, T. Lieblein, A. Bauer, O. Hertzberg, H. von Lilienfeld-Toal, and W. Mäntele, "Windowless ultrasound photoacoustic cell for *in vivo* mid-IR spectroscopy of human epidermis: Low interference by changes of air pressure, temperature, and humidity caused by skin contact opens the possibility for a non-invasive monitoring of glucose in the interstitial fluid," *Rev. Sci. Instrum.*, vol. 84, no. 8, 2013, Art. no. 084901.

[8] W. S. Lau, *Infrared Characterization for Microelectronics*. Singapore: World Scientific, 1999.

[9] M. Born and E. Wolf, *Principles of Optics: Electromagnetic Theory of Propagation, Interference and Diffraction of Light*. Amsterdam, The Netherlands: Elsevier, 2013.

[10] B. Knoll and F. Keilmann, "Near-field probing of vibrational absorption for chemical microscopy," *Nature*, vol. 399, no. 6732, pp. 134–137, May 1999.

[11] F. Keilmann, R. Hillenbrand, A. Zayats, and D. Richard, "Near-field nanoscopy by elastic light scattering from a tip," in *Nano-Optics and Near-Field Optical Microscopy*. London, U.K.: Artech House, 2009, pp. 235–265.

[12] A. Dazzi, R. Prazeres, F. Glotin, and J. Ortega, "Local infrared microspectroscopy with subwavelength spatial resolution with an atomic force microscope tip used as a photothermal sensor," *Opt. Lett.*, vol. 30, no. 18, pp. 2388–2390, 2005.

[13] A. Dazzi and C. B. Prater, "AFM-IR: Technology and applications in nanoscale infrared spectroscopy and chemical imaging," *Chem. Rev.*, vol. 117, no. 7, pp. 5146–5173, Apr. 2017.

[14] I. Rajapaksa, K. Uenal, and H. K. Wickramasinghe, "Image force microscopy of molecular resonance: A microscope principle," *Appl. Phys. Lett.*, vol. 97, no. 7, Aug. 2010, Art. no. 073121.

[15] C.-F. Wang, M. Zamkov, and P. Z. El-Khoury, "Ambient tip-enhanced photoluminescence with 5 nm spatial resolution," *J. Phys. Chem. C*, vol. 125, no. 22, pp. 12251–12255, Jun. 2021.

[16] R. M. Stöckle, Y. D. Suh, V. Deckert, and R. Zenobi, "Nanoscale chemical analysis by tip-enhanced Raman spectroscopy," *Chem. Phys. Lett.*, vol. 318, nos. 1–3, pp. 131–136, Feb. 2000.

[17] A. C. Jones and M. B. Raschke, "Thermal infrared near-field spectroscopy," *Nano Lett.*, vol. 12, no. 3, pp. 1475–1481, Mar. 2012.

[18] P. Hermann, A. Hoehl, P. Patoka, F. Huth, E. Rühl, and G. Ulm, "Near-field imaging and nano-Fourier-transform infrared spectroscopy using broadband synchrotron radiation," *Opt. Exp.*, vol. 21, no. 3, pp. 2913–2919, 2013.

[19] F. Huth, M. Schnell, J. Wittborn, N. Ocelic, and R. Hillenbrand, "Infrared-spectroscopic nanoimaging with a thermal source," *Nature Mater.*, vol. 10, no. 5, pp. 352–356, May 2011.

[20] F. Huth, A. Govyadinov, S. Amarie, W. Nuansing, F. Keilmann, and R. Hillenbrand, "Nano-FTIR absorption spectroscopy of molecular fingerprints at 20 nm spatial resolution," *Nano Lett.*, vol. 12, no. 8, pp. 3973–3978, Aug. 2012.

[21] S. Metzner, G. Wübbeler, C. Kolbitsch, and C. Elster, "A comparison of two data analysis approaches for quantitative magnetic resonance imaging," *Meas. Sci. Technol.*, vol. 33, no. 7, Jul. 2022, Art. no. 075401.

[22] W. Zhou, M. Ren, Y. Tao, L. Sun, and L. Zhu, "Enhancing the metrological performance of non-raster scanning probe microscopy using Gaussian process regression," *Meas. Sci. Technol.*, vol. 30, no. 9, Sep. 2019, Art. no. 095004.

[23] B. Kästner *et al.*, "Compressed sensing FTIR nano-spectroscopy and nano-imaging," *Opt. Exp.*, vol. 26, no. 14, pp. 18115–18124, 2018.

[24] S. Labouesse, S. C. Johnson, H. A. Bechtel, M. B. Raschke, and R. Piestun, "Smart scattering scanning near-field optical microscopy," *ACS Photon.*, vol. 7, no. 12, pp. 3346–3352, Dec. 2020.

[25] M. Marschall *et al.*, "Compressed FTIR spectroscopy using low-rank matrix reconstruction," *Opt. Exp.*, vol. 28, no. 26, p. 38762, Dec. 2020.

[26] G. Wübbeler and C. Elster, "Efficient experimental sampling through low-rank matrix recovery," *Metrologia*, vol. 58, no. 1, Feb. 2021, Art. no. 014002.

[27] G. Wübbeler, M. Marschall, E. Rühl, B. Kästner, and C. Elster, "Compressive nano-FTIR chemical mapping," *Meas. Sci. Technol.*, vol. 33, no. 3, Mar. 2022, Art. no. 035402.

[28] J. Lissajous, "Mémoire stir l'étude optique des mouvements vibratoires," *Annales de Chimie et de Physique 3e*, vol. 51, pp. 140–231, 1849.

[29] P. Hermann *et al.*, "Enhancing the sensitivity of nano-FTIR spectroscopy," *Opt. Exp.*, vol. 25, no. 14, pp. 16574–16588, 2017.

[30] S. Wundrack *et al.*, "Liquid metal intercalation of epitaxial graphene: Large-area gallenene layer fabrication through gallium self-propagation at ambient conditions," *Phys. Rev. Mater.*, vol. 5, no. 2, Feb. 2021, Art. no. 024006.

[31] M. Kruskopf *et al.*, "Comeback of epitaxial graphene for electronics: Large-area growth of bilayer-free graphene on SiC," *2D Mater.*, vol. 3, no. 4, 2016, Art. no. 041002.

[32] D. Momeni Pakdehi *et al.*, "Homogeneous large-area quasi-free-standing monolayer and bilayer graphene on SiC," *ACS Appl. Nano Mater.*, vol. 2, no. 2, pp. 844–852, Feb. 2019.

[33] D. Momeni Pakdehi *et al.*, "Minimum resistance anisotropy of epitaxial graphene on SiC," *ACS Appl. Mater. Interfaces*, vol. 10, no. 6, pp. 6039–6045, Feb. 2018.

[34] Z. Weng and X. Wang, "Low-rank matrix completion for array signal processing," in *Proc. IEEE Int. Conf. Acoust., Speech Signal Process. (ICASSP)*, Mar. 2012, pp. 2697–2700.

[35] Y. G. Peng, J. L. Suo, Q. H. Dai, and W. L. Xu, "Reweighted low-rank matrix recovery and its application in image restoration," *IEEE Trans. Cybern.*, vol. 44, no. 12, pp. 2418–2430, Dec. 2014.

[36] Q. Yao, J. T. Kwok, and W. Zhong, "Fast low-rank matrix learning with nonconvex regularization," in *Proc. IEEE Int. Conf. Data Mining*, Nov. 2015, pp. 539–548.

[37] H. W. Engl, M. Hanke, and A. Neubauer, *Regularization of Inverse Problems*, vol. 375. Berlin, Germany: Springer, 1996.
[38] P. C. Hansen, "Analysis of discrete ill-posed problems by means of the L-curve," *SIAM Rev.*, vol. 34, no. 4, pp. 561–580, Dec. 1992.
[39] M. Marschall, G. Wübbeler, and C. Elster. (2021). *Regression–Working Group 8.42*. Accessed: Jan. 12, 2022. [Online]. Available: https://www.ptb.de/cms/nc/en/ptb/fachabteilungen/abt8/fb-84/ag-842/regression-842.html
[40] E. J. Candès and Y. Plan, "Matrix completion with noise," *Proc. IEEE*, vol. 98, no. 6, pp. 925–936, Jun. 2010.
[41] T. Tuma, J. Lygeros, V. Kartik, A. Sebastian, and A. Pantazi, "High-speed multiresolution scanning probe microscopy based on Lissajous scan trajectories," *Nanotechnology*, vol. 23, no. 18, 2012, Art. no. 185501.
[42] H. Feng, H. Gu, D. Silbersweig, E. Stern, and Y. Yang, "Single-shot MR imaging using trapezoidal-gradient-based Lissajous trajectories," *IEEE Trans. Med. Imag.*, vol. 22, no. 8, pp. 925–932, Aug. 2003.
[43] A. Bazaei, Y. K. Yong, and S. O. R. Moheimani, "High-speed Lissajous-scan atomic force microscopy: Scan pattern planning and control design issues," *Rev. Sci. Instrum.*, vol. 83, no. 6, 2012, Art. no. 063701.
[44] X. Sun, E. Heaps, A. Yacoot, Q. Yang, P. Grolich, and P. Klapetek, "Three-dimensional drift correction of scan data from atomic force microscopy using Lissajous scanning paths," *Meas. Sci. Technol.*, vol. 32, no. 11, Nov. 2021, Art. no. 115010.
[45] F. Werner, N. Gdaniec, and T. Knopp, "First experimental comparison between the Cartesian and the Lissajous trajectory for magnetic particle imaging," *Phys. Med. Biol.*, vol. 62, no. 9, p. 3407, 2017.
[46] H. Lin, C.-S. Liao, P. Wang, N. Kong, and J.-X. Cheng, "Spectroscopic stimulated Raman scattering imaging of highly dynamic specimens through matrix completion," *Light: Sci. Appl.*, vol. 7, no. 5, p. 17179, 2018.

Selma Metzner received the Ph.D. degree from the Technical University of Berlin, Berlin, Germany, in 2021, with a focus on applying Bayesian approaches to high-dimensional medical imaging data.

She was a Post-Doctoral Researcher with the Working Group Data Analysis and Measurement Uncertainty, Physikalisch-Technische Bundesanstalt (PTB), Braunschweig, Germany. Her research interests include Bayesian statistical methods for large-scale data analysis.

Bernd Kästner received the Ph.D. degree from the Hitachi Cambridge Laboratory, Cambridge University, Cambridge, U.K., in 2004, with a focus on lateral p-n junctions.

From 2004 to 2006, he was a Researcher in the field of single-electron transport with the National Physical Laboratory, Teddington, U.K. In 2006, he joined the Physikalisch-Technische Bundesanstalt (PTB), Braunschweig, Germany, where he is involved in non-adiabatic single-electron-quantized current sources. In 2013, he joined PTB and the Metrology Light Source (MLS), Berlin, Germany, where he is involved in developing infrared (IR) and THz spectroscopy techniques. He is currently the head of a working group in the field of IR and THz near-field microscopy. His research interests include nanoscale contactless electrical characterization, thermoelectric scanning probe microscopy, and compressed Fourier transform infrared (FTIR) spectroscopy.

Manuel Marschall received the Ph.D. degree from the Weierstrass Institute for Applied Analysis and Stochastics, Technical University of Berlin, Berlin, Germany, in 2020, with a focus on explicit and adaptive Bayesian inversion in hierarchical tensor format.

He is currently a Post-Doctoral Researcher with the Working Group Data Analysis and Measurement Uncertainty, Physikalisch-Technische Bundesanstalt (PTB), Braunschweig, Germany. His research interests include the field of statistical data analysis with a focus on large-scale Bayesian approaches.

Gerd Wübbeler received the Diploma and Ph.D. degrees in experimental solid-state physics from the University of Osnabrück, Osnabrück, Germany, in 1990 and 1995, respectively.

Dr. Wübbeler is a member of the Working Group Data Analysis and Measurement Uncertainty, Physikalisch-Technische Bundesanstalt (PTB), Braunschweig, Germany, and has a long-standing expertise in statistical data analysis for metrological applications and quantitative imaging.

Stefan Wundrack was born in Magdeburg, Germany, in 1985. He received the Diploma degree in analytical chemistry from the Max Planck Institute for Dynamics of Complex Technical Systems, Magdeburg-Stendal University of Applied Sciences, Magdeburg, Germany, in 2008. He is currently pursuing the Ph.D. degree in the research field of epitaxy of confined 2-D materials with epitaxial graphene with the Institute of Semiconductor Technology, Technical University of Braunschweig (TU Braunschweig), Braunschweig, Germany, in 2020.

In 2010, he joined the Physikalisch-Technische Bundesanstalt, Braunschweig, Germany, where he is currently with the Chemical Surface Analysis Group. He is responsible for the metrological linkage of optical vibrational spectroscopy techniques (e.g., Raman spectroscopy) to the SI system. His research interests include the preparation of transition metal dichalcogenides via CVD fabrication for technical and metrological applications.

Andrey Bakin received the Ph.D. degree from Saint Petersburg Electrotechnical University, Saint Petersburg, Russia, in 1985.

In 1998, he joined the Institute of Semiconductor Technology, Technical University of Braunschweig, Braunschweig, Germany, where he is an extraordinary Professor. His current research interests include thin-film technologies of compound materials, 2-D materials and their stacks, liquid metal intercalation, nanotechnology, and plasma profiling time-of-flight mass spectrometry.

Arne Hoehl received the pre-degree in physics from Martin-Luther-University Halle-Wittenberg, Halle, Germany, in 1996, and the Diploma (graduate) degree in physical engineering and technology from the University of Applied Sciences Jena, Jena, Germany, in 2002, with a focus on physics-intensive technologies and laser sciences.

In 2003, he joined the Radiometry Laboratory, Physikalisch-Technische Bundesanstalt (PTB), Braunschweig, Germany, at the electron storage ring BESSY II, Berlin, Germany. He is currently a Senior Engineer with the Working Group Infrared (IR) Spectroscopy, PTB, mainly at the electron storage ring Metrology Light Source, Berlin.

Eckart Rühl received the Ph.D. degree in chemistry and the Habilitation degree in physical chemistry from Freie Universität Berlin, Berlin, Germany, in 1987 and 1993, respectively.

He was a Professor of physics with Johannes Gutenberg Universität Mainz, Mainz, Germany, and a Full Professor of environmental physics with Universität Osnabrück, Osnabrück, Germany. He was a post-doctoral researcher in France (Orsay, Meudon), U.K. (Oxford), Canada (Hamilton), and USA (Boulder). He was the Chair of Physical Chemistry I with Julius-Maximilians-Universität Würzburg, Würzburg, Germany. He has been a Full Professor of physical chemistry with Freie Universität Berlin since 2006. His scientific work is documented in more than 280 publications mostly in the field of spectroscopy.

Clemens Elster received the Ph.D. degree from Freiburg University, Freiburg im Breisgau, Germany, in 1993, with a focus on designing methods for experimental design and the optimization of noisy functions.

He is leading the Working Group Data Analysis and Measurement Uncertainty, Physikalisch-Technische Bundesanstalt (PTB), Braunschweig, Germany. His research interests include the field of statistical data analysis with a focus on Bayesian approaches and methods for deep learning.